

---

## Hot Deformation Behavior of a Nickel-modified AISI 4330 Steel

Matthieu BITTERLIN,<sup>1)</sup> Davood SHAHRIARI,<sup>1)</sup> Louis-Philippe LAPIERRE-BOIRE,<sup>2)</sup> Jean-Benoît MORIN<sup>2)</sup> and Mohammad JHAZI<sup>1)\*</sup>

1) École de Technologie Supérieure, Department of Mechanical Engineering, 1100 Notre-Dame Street West, Montreal, QC, H3C 1K3, Canada.

2) Finkl Steel-Sorel, 100 McCarthy, Saint-Joseph-de-Sorel, QC, J3R 3M8, Canada.

*(Received on January 24, 2018; accepted on May 17, 2018; J-STAGE Advance published date: July 28, 2018)*

---

## **Hot deformation behavior of a nickel-modified AISI 4330 steel**

M. Bitterlin <sup>a</sup>, D. Shahriari <sup>a</sup>, L.-P. Lapierre-Boire <sup>b</sup>, J.-B. Morin <sup>b</sup>, M. Jahazi <sup>a\*</sup>

<sup>a</sup> École de Technologie Supérieure, Department of Mechanical Engineering, 1100 Notre-Dame Street West, Montreal, QC, H3C 1K3, Canada

<sup>b</sup> Finkl Steel-Sorel, 100 McCarthy, Saint-Joseph-de-Sorel, QC, J3R 3M8, Canada

\* corresponding author

M. Jahazi : [mohammad.jahazi@etsmtl.ca](mailto:mohammad.jahazi@etsmtl.ca)

## **Synopsis**

Hot compression of a nickel-modified AISI 4330 steel was studied over a wide range of temperatures and strain rates using Gleeble 3800 thermomechanical simulator. Samples were quenched at different stages of deformation to study microstructure evolution using optical and electron microscopies. Stress-strain curves showed that both dynamic recovery (DRV) and dynamic recrystallization (DRX) take place for certain deformation conditions. However, in comparison to low alloyed steels with lower nickel content, the nickel-modified AISI 4330 steel showed significantly lower workability particularly, resulting from the temperature and strain rate ranges over which DRX takes place. The kinetics of recrystallization were studied and the stress constants and apparent activation energies were determined for the investigated alloy and compared with similar alloy with lower nickel content so as to quantify the influence of nickel. The obtained results are interpreted in terms of the influence of nickel on dislocation dynamics and therefore the softening process at high temperature under various ranges of strain rate. The findings will help a better design of the forging process of these alloys which are prone to hot cracking during open die forging.

Key words : high nickel content low alloy steels; flow stress; constitutive modeling; thermomechanical processing; dynamic recrystallization; workability.

## 1. Introduction

AISI 4330 steel grade, also known as CrNiMoV steel, is widely used in the aerospace industry, especially in rotor engine components <sup>1)</sup>, because of its high strength and good wear resistance <sup>2-5)</sup>. In recent years, its applications in critical equipment used in the oil and gas industry have been on the rise. However, for certain specific applications, lower ductile-brittle transition temperatures or higher strength and wear resistance are required which can't be achieved with conventional AISI 4330 steel. The presence of nickel in the composition of this steel reduces the ductile-fragile transition temperature <sup>1)</sup>, while the addition of chromium strengthens the material and improves its wear resistance <sup>1, 3)</sup>. Industry is contemplating new higher content nickel and chromium alloys in order to attain the required properties. The most important change in the composition of these alloys has been the addition of a higher amount of nickel. However, such modifications impact the phase compositions and high temperature formability of the alloy that need to be addressed <sup>6-11)</sup>. Specifically, it has been reported that nickel-containing steels are sensitive to cracking during the hot forging process <sup>9, 10)</sup>. Considering that the rotor shaft manufacturing process generally consists in ingot casting followed by open-die forging in multiple steps, it is therefore critical to study the hot forming behavior of these steels.

Several factors have been reported as being at the root of the observed cracking, including second-phase embrittlement by decohesion or oxidation at grain boundaries <sup>9, 10)</sup>, segregation <sup>10, 11)</sup>, and large grain size <sup>9)</sup>. Alone or in combination, all these factors can affect grain cohesion, and thus, the material toughness and are significantly dependent on hot working parameters <sup>9)</sup>. On the other hand, it has been reported that the crack growth resistance of AISI 4330 steel is improved by the formation of metastable microstructures

such as upper and lower bainite <sup>4, 5)</sup>, which is also dependent on the selection of high temperature processing parameters. Hence, a better understanding of the mechanisms governing microstructure evolution during open-die forging of these alloys would allow the optimum design of the thermomechanical process, and could help in developing suitable microstructures and minimize or avoid the observed cracking <sup>1, 2, 9)</sup>.

It is well known that during hot working, softening mechanisms such as dynamic recovery (DRV) and dynamic recrystallization (DRX), which could have a determining effect on the selection of thermomechanical processing parameters <sup>7, 12-15)</sup>, take place and modify the microstructure. In general, the mechanical behavior and microstructure evolution of materials at high temperatures can be studied using constitutive equations for recrystallization <sup>12-16)</sup>. Of the various existing models, the Arrhenius model has proven to be very consistent in predicting the behavior of medium carbon low alloyed steels <sup>16)</sup>. The Arrhenius equation allows determining the apparent activation energy of deformation, which is then used to quantitatively compare the workability of the alloy, as discussed by McQueen and Ryan <sup>17)</sup>. Many authors have used this method and concluded that alloying elements have a non-negligible influence on the apparent activation energy value, as compared to the self-diffusion of austenite in pure iron <sup>12, 14, 15, 17)</sup>. While the influence of minor additions of Ti, Nb, and V on the kinetics of DRV and DRX has been extensively studied <sup>13, 14)</sup>, very few studies are however available on the role of nickel and its possible influence on the kinetics of DRV and DRX needs to be quantified.

The objective of this study is therefore to investigate the influence of nickel on the high temperature flow behavior of nickel-modified AISI 4330 steel. To this end, hot compression tests were conducted in a wide range of strain rate and deformation

temperatures, simulating the industrial process. The experimental stress-strain curves were analyzed, constitutive equations of the material mechanical behavior at high temperature were developed, and the kinetics of recrystallization were determined. The obtained results are compared to steels with similar compositions and discussed in order to highlight the influence of nickel on the high temperature behavior of medium carbon steels.

## **2. Experimental procedure**

The flow behavior of nickel-modified AISI 4330 steel was studied using isothermal compression tests under a wide range of temperatures and strain rates corresponding to the industrial forging process for large size ingots. Samples used in the present study were collected and provided by Finkl Steel Inc., Quebec, Canada. The nominal composition of the steel is given in **Table 1**. Cylindrical specimens 15mm in height and 10mm in diameter were machined from a forged 142cm diameter ingot. Isothermal hot compression tests were conducted on a Gleeble-3800 thermo-simulation machine covering a range of seven different temperatures (1223, 1273, 1323, 1373, 1423, 1473 and 1523K) and four strain rates (0.01, 0.1, 0.5 and  $1\text{s}^{-1}$ ). Each specimen was heated using a thermo-coupled feedback-controlled AC current at a  $2\text{K}\cdot\text{min}^{-1}$  heating rate and held at 1573K for 5 minutes in order to obtain homogenous temperature distribution over the specimen, before being cooled at a rate of  $1\text{K}\cdot\text{min}^{-1}$  to the forming temperature. A 60% height reduction was recorded at the end of compression tests. Temperature distribution was measured using K-type thermocouples spot-welded to the center region

of the specimen surface and protected by ceramic tubes in order to avoid a misreading of the temperature due to element diffusion in the thermocouple. All samples were air-quenched after the thermomechanical cycle, and used for microstructural investigation. **Figs. 1a and b** schematically illustrate the deformation process on the Gleeble machine and the experimental setup for the instrumented compression sample, respectively.

The deformed samples were cut along the compression axis and mechanically polished using different SiC paper up to 1200 grit followed by 1 $\mu$ m diamond paste as the final polishing step. Revealing the prior austenite grain size of the as deformed samples revealed quite challenging. Interestingly, very few or no published data is available on metallographic methods for revealing the recrystallized austenite grains in medium carbon low alloy steels with bainitic microstructures. An extensive number of experiments, including etching, heat tinting, and combined etching and heat treatment, were carried out to determine the best conditions for revealing the contours of the grains in as deformed samples. Among the various tested methods, chemical etching with the solutions and etching times as reported in **Table 2**<sup>18)</sup> were successful. Microstructural observations were made at the center of the samples using optical and scanning electron microscopy.

### **3. Results**

The starting microstructure was revealed using 3%wt Nital solution, and is presented in **Fig. 1c**. The microstructure was bainitic with bainite laths with different dimensions clearly visible under microscope. The boundaries of the prior austenite grains were barely

visible after etching; however, using the different orientations of bainite laths, it was possible to trace the boundaries and determine the average prior austenite grain size of the starting material to be about  $89\mu\text{m}$  ( $\pm 10\mu\text{m}$ ).

The stress-strain curves obtained for the different temperatures and strain rates are shown in **Fig. 2**. It can be seen that for all seven test temperatures, the flow stress increases as the strain rate increases and/or the temperature decreases. Also, the presence of a peak stress observed above 1423K, at strain rate of  $0.1\text{s}^{-1}$ , is indicative of the occurrence of dynamic recrystallization <sup>7, 12, 14, 15, 19</sup>.

**Figs. 3a, b and c** show macrostructures for different conditions using **Table 2** etchants of deformed samples. The corresponding SEM micrographs are presented in **Figs. 3d, e and f**, respectively. Using the SEM micrographs, it was also possible to identify the grain boundaries, as highlighted in the figures. The results in **Figs. 3e and f** clearly indicate the formation of significantly smaller and more equiaxed grains in the as-deformed samples at temperatures of 1423K and 1523K at  $0.01\text{s}^{-1}$ , also illustrated by reduced stress levels on stress-strain curves in **Fig. 5a** compared to the as-received ones. The above findings are in agreement with previous research indicating the occurrence of DRX in Ni-containing steels <sup>7, 12, 16, 17</sup>. In contrast, microscopic observations of deformed sample at 1473K and  $1\text{s}^{-1}$  in **Fig. 3d** presents larger grains compared to **Figs. 3e and f**. The affiliate stress-strain curve in **Fig. 5d** shows that no softening and stress drop is observed, implying that DRX doesn't occur for this condition.

A further analysis of the curves indicated that at 1523K, the peak strain passed from 0.15 to 0.3 as the strain rate was increased from  $0.1\text{s}^{-1}$  to  $1\text{s}^{-1}$  (**Fig 2b and d**). In contrast, at

temperatures below 1373K, it appears that the stress continues to increase even at a lower strain rate, however no evidence of work hardened microstructure was observed during microscopic analyses (e.g. see **Fig. 3d**), indicating that only recovery occurred under the examined conditions and the observed increase in stress levels could be related to frictional effects <sup>20)</sup>. Therefore, the stress-strain curves need to be corrected as friction may occur and change the shape and levels of stress.

### 3.1. Friction correction

**Fig. 4** is an illustrative example of the geometry of as-deformed sample to a strain of 0.85 at temperature of 1223K and strain rate of  $0.01\text{s}^{-1}$ . Deformed specimens in **Figs. 3a, b and c** show heterogeneous deformation zones : no deformation zones on each flat sides of the specimen, moderate deformation of the barreled sides (central radius,  $R_m$ , larger than the top one,  $R_t$ ) and intense shearing on a cross section of the specimen. These findings are in agreement with those of previous authors, highlighting that the specimen underwent friction during hot deformation <sup>20)</sup>.

The lubricant generally loses its efficiency as the temperature or duration of the test increases, resulting in an increase in stress at high strains. Several mathematical relations have been proposed in the literature in order to compensate for the friction effect <sup>21, 22)</sup>. In the present work, the constant friction factor model proposed by Dieter <sup>23)</sup> was used as it has been successfully applied to steels:

$$\sigma = \frac{C^2 P}{2[\exp(C)-C-1]} \quad (1)$$

where,  $C = \frac{2\mu r}{h}$ ,  $\sigma$  is the stress without friction (MPa),  $P$  is the flow stress with friction (MPa),  $\mu$  is the constant friction factor,  $r$  and  $h$  are respectively the instantaneous radius and height of the sample (mm). The constant friction factor was determined using the barreling factor of each sample based on the following relations<sup>21, 22</sup>:

$$\mu = \frac{R_{th}/h \cdot b}{4/\sqrt{3} - 2b/3\sqrt{3}} \quad (2)$$

$$b = 4 \frac{\Delta R}{R_{th}} \cdot \frac{H}{\Delta H} \quad (3)$$

where  $b$  is the barreling factor,  $\Delta R$  is the difference between the maximum ( $R_m$ ) and the top radius ( $R_t$ ) of the specimen (mm),  $R_{th}$  is the theoretical radius of the sample based on the volume conservation in friction-free conditions (mm),  $\Delta H$  is the height reduction of the sample during hot compression tests (mm), and  $H$  and  $R$  are the final height and radius of the sample after hot compression testing, respectively (mm).

The friction-corrected stress-strain curves are presented in **Fig. 5**. It can be seen that recrystallization occurs only at temperatures higher than 1373K for strain rates above  $0.1s^{-1}$ . At temperatures below 1373K and strain rates more than  $0.1s^{-1}$ , the stress is stabilized at a constant value, highlighting the occurrence of softening due to recovery. In contrast, at low strain rates ( $0.01s^{-1}$ ), recrystallization occurs even at 1223K, as shown in **Fig. 5a**.

### 3.2. Determination of apparent activation energy for deformation

Apparent activation energy provides information about the workability of the material, and can be compared to other steels in order to explain the observed differences in hot forming behavior<sup>12, 14, 15, 17)</sup>. The Arrhenius constitutive model has been widely used to correlate, with good accuracy, the flow stress behavior of materials when diffusion-controlled phenomena such as DRV and DRX take place<sup>12, 14, 15, 17)</sup>. Material constants needed in the constitutive model can be determined by deriving stress-strain data obtained through compression testing. The Arrhenius model is based on the Zener-Hollomon parameter<sup>12, 14-17)</sup>:

$$Z = \dot{\epsilon} \exp\left(\frac{Q}{RT}\right) \quad (4)$$

where, the strain rate can be described using the following relation:

$$\dot{\epsilon} = AF(\sigma_p) \exp\left(\frac{-Q}{RT}\right) \quad (5)$$

in which:

$$F(\sigma_p) = \begin{cases} \sigma_p^{n'} & \alpha\sigma > 0.8 \text{ (low stress levels)} \\ \exp(\beta\sigma_p) & \alpha\sigma < 1.2 \text{ (high stress levels)} \\ [\sinh(\alpha\sigma_p)]^n & \text{for all } \alpha \text{ (all stress levels)} \end{cases} \quad (6)$$

In the above equation,  $\dot{\epsilon}$  is the strain rate ( $s^{-1}$ ),  $\sigma_p$  is the peak stress,  $Q$  is the apparent activation energy for deformation of the material ( $kJ.mol^{-1}$ ),  $R$  is the universal gas constant ( $8.314 J.mol^{-1}.K^{-1}$ ),  $T$  is the temperature (K), and  $A$ ,  $n'$ ,  $n$ ,  $\beta$ ,  $\alpha$  are material constants.  $\alpha$  is a parameter that can be determined using the following equation<sup>12, 14-17)</sup>:

$$\alpha = \frac{1}{n'} \times \beta \quad (7)$$

The experimental peak stresses of each stress-strain curve were determined using the Poliak and Jonas method of double differentiation<sup>24)</sup> after polynomial fitting was applied (in gray in **Fig. 5**). In the present study, a 9<sup>th</sup> order polynomial fitting proved to be successful, as Pearson's coefficient was above 0.999 for all experimental conditions. In order to obtain work hardening curves the derivatives of the polynomial fitting were then obtained and the results are shown in **Fig. 6** :

$$\theta = \frac{\delta\sigma}{\delta\varepsilon} \quad (8)$$

The peak stress value was reached when the work hardening  $\theta = \frac{\delta\sigma}{\delta\varepsilon} = 0$  on strain hardening curves  $\theta$ - $\sigma$  (**Figs. 6**), whereas the critical stress was determined graphically as the minima of the  $\left| -\frac{\delta\theta}{\delta\sigma} \right|$  curve<sup>24, 25)</sup> as it can be seen in **Fig. 6a**.

By taking the logarithms of Eqs. (6),  $n'$ ,  $\beta$  and  $n$  values can be determined:

$$\ln \dot{\varepsilon} = \begin{cases} \ln A_1 + n' \ln \sigma_p - \frac{Q}{RT} \\ \ln A_2 + \beta \sigma_p - \frac{Q}{RT} \\ \ln A + n \ln[\sinh(\alpha \sigma_p)] - \frac{Q}{RT} \end{cases} \quad (9)$$

Material constants  $n'=5.7415$ ,  $\beta=0.0863 \text{ MPa}^{-1}$  were determined from the slope of  $\ln\sigma_p$ - $\ln\dot{\epsilon}$  (**Fig. 7a**) and  $\sigma_p$ - $\ln\dot{\epsilon}$  (**Fig. 7b**) curves, respectively. As a result,  $\alpha$  was determined to be equal to 0.015. Finally,  $n$  was determined to be equal to 4.2360 using the slopes of  $\ln(\sinh(\alpha\sigma_p))$ - $\ln\dot{\epsilon}$  (**Fig. 7c**) curves.

Using the following equation, the apparent activation energy,  $Q$ , was determined from the linear regressions of the plots of  $\ln(\sinh(\alpha\sigma_p))-1/T$  at different strain rates (**Fig. 7d**). The calculation led to a  $Q$  value of  $367.927 \text{ kJ.mol}^{-1}$  which is about 31% higher than the deformation activation energy of pure austenite <sup>17)</sup>, but is in the range of  $280 \text{ kJ.mol}^{-1}$  –  $384 \text{ kJ.mol}^{-1}$  of medium carbon low alloy steels apparent activation energies reported by other researchers <sup>6, 14, 15)</sup>.

$$Q = nR \frac{\delta \ln[\sinh(\alpha\sigma)]}{\delta(\frac{1}{T})} \quad (10)$$

### 3.3. Kinetics of recrystallization

The experimental curves at temperatures above 1423K in **Figs. 5 and 6** and **Table 3** indicate the occurrence of dynamic recrystallization. At high temperatures, the steel is principally composed of austenite phase, which has strong dynamic recrystallization tendency because of its low stacking fault energy <sup>12, 26, 27)</sup>. This stacking fault energy can increase in the presence of alloying elements, as has been reported by other researchers <sup>12, 17)</sup>. Thus, the initiation of DRX and its kinetics could be moved to higher temperatures

and/or lower strain rates in the presence of alloying elements as it can be observed in **Table 3**. Such an impact is quantified using Avrami equation as indicated in Eq. (11) <sup>15, 25-29</sup>).

$$X = 1 - \exp(-kt^{n_{DRX}}) = 1 - \exp\left[-k\left(\frac{\varepsilon - \varepsilon_c}{\varepsilon_p}\right)^{n_{DRX}}\right] \quad (11)$$

where  $X$  is the recrystallization fraction,  $\varepsilon_c$  and  $\varepsilon_p$  are the critical and the peak strain, respectively;  $k$  and  $n_{DRX}$  are dynamic recrystallization parameters corresponding to the Avrami constant and the time exponent, respectively. The constant  $n_{DRX}$  is independent of temperature, and can vary from 1 to 4, whereas  $k$  depends on the nucleation and growth rates  $N$  and  $v$ , which are functions of temperature <sup>28</sup>):

$$k = \frac{\pi N v^3}{3} \quad (12)$$

To calculate the  $n_{DRX}$  and  $k$  values, the first part of Eq. (11) can be rearranged as:

$$\ln[-\ln(1 - X)] = n_{DRX} \ln t + \ln k \quad (13)$$

Therefore,  $n_{\text{DRX}}$  and  $k$  values can be determined from the slope and the intercept of the relations between  $\ln(-\ln(1-X))$  and  $\ln t$ , respectively. The fraction of dynamically recrystallized grains,  $X$ , was determined experimentally using the stress-strain curves in **Fig. 5** and the following equation<sup>15, 25, 27, 29)</sup>:

$$X = \frac{\sigma_p - \sigma}{\sigma_p - \sigma_{ss}} \quad (14)$$

where  $\sigma_p$  is the peak stress and  $\sigma_{ss}$  is the steady-state stress, which is the mean value of stress after completion of DRX. As detailed previously, experimental critical and peak stresses values were determined using the double differentiation method<sup>24)</sup>. The peak stress corresponds to the state where softening takes over work hardening as the main governing mechanism, and it can therefore be related to the peak strain  $\varepsilon_p$ . However, the critical strain  $\varepsilon_c$  is the deformation at which the first nuclei of recrystallized grain is formed<sup>26, 27)</sup>. The double differentiation method was also used in order to determine the steady-state stress. When dynamic recrystallization occurs, the work hardening curve  $\theta$ - $\sigma$  is characterized by a negative slope until it reaches  $\theta=0$ . Then, the curve follows a complete loop until it reaches again  $\theta=0$  at a lower stress value. This latter value is set to be the steady-state stress<sup>25, 27)</sup>.

**Figs. 8a and b** show that a linear relation exists between  $\varepsilon_c$  and  $\varepsilon_p$ , and  $\sigma_c$  and  $\sigma_p$ , respectively. It can be seen that the relation between the critical and peak stress ratios

(**Fig. 8b**) provides a better Pearson's coefficient as compared to that between the critical and peak strain ratios (**Fig. 8a**).

Finally, the mean slope  $n_{\text{DRX}}$  and the intercept  $k$  of Eq. (13) of the experimental curves data were determined to be 4.1798 and 0.5504, respectively. Therefore, Eq. (11) can be rewritten as:

$$X = 1 - \exp(-0.5504t^{4.1798}) \quad (15)$$

To evaluate the precision of the determined kinetics of DRX of nickel-modified AISI 4330 steel, the calculated  $X$  data from Eq. (15) were compared to experimental data from the stress-strain curves of **Fig. 5** and reported in **Fig. 9**.

An examination of **Fig. 9** shows that the model shows quite good agreement with experimental recrystallization fraction values, and can therefore be used to describe the evolution of DRX of the studied steel. However, some differences between the established model and the experimental DRX kinetics appear. It can be seen on **Fig. 9b** that the predicted curve for 1423K is delayed to higher strain compared to experimental dots. This could be attributed to the use of average values of Avrami's constant  $k$  and exponent  $m$ , as also noted by other researchers<sup>14, 27</sup>.

## 4. Discussion

### 4.1 Microstructure analyses

The width of grain boundaries are submicron scale even under high resolution scanning electron microscopy, making the grain size analyses quite complex. As stated, many reagents and chemical solutions were tested but none could reveal completely the grain boundaries of deformed samples or as-received microstructure. Therefore, prior austenite grain boundaries of specimens were redrawn in order to evaluate dynamic mechanisms occurring under several deformation conditions. Only, the prior austenite grain boundaries of quenched and tempered samples could be revealed by chemical etching or heat tinting. Therefore, further investigations need to be realized in order to determine a suitable technique for revealing prior austenite grain boundaries in nickel rich low alloy bainitic steels under as-forged conditions.

As shown in **Figs. 3e and f**, the bainite laths form equiaxed substructures which indicates that no work hardening has occurred at 1423K and  $0.01s^{-1}$ , and 1523K and  $0.01s^{-1}$  respectively<sup>19)</sup>. Moreover, the absence of ferrite laths in the deformed samples indicated that the observed stress reduction on the stress-strain curves could only be due to dynamic recrystallization. Finally, as it can be seen in **Fig. 3d**, grain size is significantly larger than in **Figs. 3e and f**. Hence, as illustrated in **Fig. 6d**, no work hardening loop is observed using double differential method, which indicates that no softening due to DRX took place in the material<sup>29)</sup>. The above findings indicate that no dynamic recrystallization occurred at 1473K and  $1s^{-1}$ . Therefore, it can be concluded that dynamic recovery is the principal softening mechanism occurring during hot deformation at

1473K at  $1\text{s}^{-1}$  (**Fig. 3d**, **Fig. 5d** and **Fig. 6d**). A summary of the analyses regarding the occurrence of dynamic mechanisms in deformed samples is reported in **Table 3**.

#### 4.2 Apparent activation energy and stress levels

Apparent activation energy has already been used as an indicator of flow stress behavior of materials under hot deformation <sup>27, 29</sup>. **Table 4** compares the apparent activation energies and material constants of similar steels, albeit with lower nickel contents <sup>12, 30</sup>. The findings in the present investigation show that nickel increases the stress multiplier  $\alpha$  from approximately  $0.010\text{ MPa}^{-1}$  to  $0.015\text{ MPa}^{-1}$ , and inversely, decreases the stress exponent  $n$  from values around 7–8 to 4.23 (**Fig. 10a**). On the influence of alloying elements on  $\alpha$ , McQueen and Ryan <sup>17</sup>) found that low alloyed steels exhibit lower average  $\alpha$  values ( $\alpha=0.012 - 0.014\text{ MPa}^{-1}$ ) than stainless steels ( $\alpha=0.0172 - 0.0254\text{ MPa}^{-1}$ ), and suggested that this effect is essentially due to solute element alloying and chromium content. In **Figs. 10a and b**, it can be seen that as the nickel content increases, the material constants  $\alpha$  and  $n$  increase and decrease, respectively. Moreover, the apparent activation energy decreases from  $490.749\text{ kJ.mol}^{-1}$  to  $367.927\text{ kJ.mol}^{-1}$  with nickel alloying increased to 2.89%wt, representing a 8.66% decrease by %wt nickel alloying (**Fig. 10b**). The same effect has been observed by previous authors with carbon alloying <sup>31</sup>). Mead and Birchenall observed a 35% apparent activation energy decrease by increasing carbon content from 0.024 to 0.54%wt in a 0.5Mn-0.25Si steel <sup>32</sup>). Sakai *et al.* had also observed that in a 0.5Mn-0.5Si steel, by increasing the carbon content from

0.036 to 0.53%wt, the apparent activation energy decreased from 309 to 270 kJ.mol<sup>-1</sup>, representing a 24% decrease<sup>33)</sup>. However, in the two above studies, the authors noted that the apparent activation energy remained stable when the carbon content went over 0.5%wt<sup>32, 33)</sup>.

It is important to note that, the decreasing apparent activation energy with the increase in nickel content contrasts with the increase of the DRX start temperature with the nickel content. As the recrystallization start temperature increases with the nickel content (**Fig. 10b**), the activation energy is expected to be higher because the stacking fault energy is increased due to higher amounts of the substitutional alloying elements<sup>12, 15, 17)</sup>. In the Arrhenius model, the microstructure is assumed to remain constant through high temperature deformation cycle. As a result, the activation energy determined using the present model can only be considered as apparent, because heat input and deformation can modify the grain size and the subgrain size, and therefore the microstructure<sup>17)</sup>. As can be seen in Eq. (10), Q is directly related to n, and therefore, to material constant  $\alpha$ <sup>12, 14-17, 28-30, 34)</sup>. Furthermore, as also reported by others, as a higher  $\alpha$  implies a lower n value, therefore, the apparent activation energy is reduced or increased as a function of Arrhenius parameters<sup>17, 24, 34)</sup>. For example, Matuszewski *et al.*<sup>34)</sup> calculated an apparent activation energy value of 253 kJ.mol<sup>-1</sup> for 50B44 boron steel while Wang *et al.*<sup>35)</sup> reported a value of 378.6 kJ.mol<sup>-1</sup> for medium carbon manganese steel. It should be noted that the  $\alpha$  values were higher in the boron steel than in the carbon steel, while in contrast, the n exponent of the boron steel was much lower, resulting in overall lower Q values. Therefore, because the stress exponent n of modified AISI 4330 steel (n=4.2360) is much lower than those for AISI 4130 (n=7.077) and AISI 4340 (n=7.74) steels (**Fig. 10a**), a

lower workability is expected for the nickel-modified AISI 4330 steel. Also, under these conditions, the actual activation energy of the nickel-modified AISI 4330 steel should then be higher than the apparent activation energy found using the Arrhenius model<sup>12, 30, 35</sup>).

### 4.3 Recrystallization kinetics

The occurrence of DRX is mainly governed by the mutual influences of temperature and strain rate. At higher strain rates, the annihilation rate of dislocations decreases, and therefore, DRV is favored instead of DRX, as illustrated in **Fig. 5** for test temperatures below 1423K. As can be seen in **Figs. 9a, b, c and d**, by increasing the temperature, the critical strain for the initiation of recrystallization is decreased, thereby accelerating the kinetics of recrystallization (slopes of X curves). For example, from 1223K to 1273K and strain rate of  $0.01\text{s}^{-1}$ , the 50% fraction recrystallized is reduced from a strain of 0.55 to 0.42 (**Fig. 9a**). In contrast, strain rate has the inverse effect of temperature. At 1423K, as the strain rate increases from  $0.01\text{s}^{-1}$  to  $0.1\text{s}^{-1}$  the 50% fraction recrystallized strain changes from 0.25 to 0.45 (**Figs. 9a and b**).

As reported in **Fig. 8**, a linear relation exists between critical and peak stress and strain. The above results are in agreement with those reported by other researchers who observed such linear relations between the critical and peak stress and strain ratios<sup>12, 15, 25, 26</sup>). It is worth noting that some authors reported that the relation between peak and

critical strain has a lower Pearson's coefficient than the stress relation, and related it to the use of the double differential method <sup>27)</sup>.

It can be seen in **Table 5** and **Fig. 11** that alloying elements have a significant influence in terms of slowing down the kinetics of DRX, as the Avrami's constant  $k$  decreases with the addition of vanadium, niobium, and nickel. The lower value of the constant  $k$  reflects the decreased nucleation and growth rate of recrystallized grains, as shown in Eq. (12) <sup>28)</sup>. For example, Zhu *et al.* <sup>15)</sup> and Zhang *et al.* <sup>29)</sup> reported that the addition of 0.036%wt niobium reduces the Avrami parameter from 0.695 to 0.62 in a 34CrNiMo steel and inversely increases the apparent activation energy by 11% and the DRX start temperature from 1223K to 1273K at the same strain rate <sup>15,29)</sup>. Akben *et al.* <sup>36)</sup> noted that niobium has a ten times stronger retardation power on static recrystallization than molybdenum. This value increases to twenty times for vanadium. This delay in recrystallization translates into a 44% increase in the strengthening effect of austenite, as compared to 5% and 8% for molybdenum and vanadium, respectively.

#### 4.4 Influence of nickel on dynamic mechanisms of softening and workability

In order to study the workability of nickel-modified steel, strain rate sensitivity values can be obtained from the slopes of  $\ln\sigma$ - $\ln\dot{\epsilon}$  curves (**Fig. 7a**) <sup>12, 17)</sup>. The strain rate sensitivity  $m$  is defined as :

$$\frac{\partial \ln \sigma}{\partial \ln \dot{\epsilon}} = \frac{1}{n'} = m \quad (16)$$

The strain rate sensitivity represents the amount of stress increase relative to strain rate increase. This amount and the dynamic mechanisms occurrence by increasing strain rate can create stress variations in the material, resulting in different response to deformation during hot forging. **Fig. 12** shows that the nickel-modified AISI 4330 steel is significantly sensitive to strain rate than lower nickel-content AISI 4130 and AISI 4340 steels. The average values at 1223K are between 0.15 and 0.19, whereas for lower nickel alloyed steels, the strain rate sensitivity doesn't exceed 0.15. The above results reveal that the stress increase with strain rate of the nickel-modified AISI 4330 steel is higher than that of the lower nickel content steel. For example, at 1373K, by increasing the strain rate from  $0.01 \text{ s}^{-1}$  to  $0.1 \text{ s}^{-1}$ , the peak stress of nickel-modified AISI 4330 changes from 41.9 MPa to 70.135 MPa, representing a 67.4% stress increase. In comparison, under the same conditions, AISI 4130 steel peak stress increases from 40MPa to 60MPa, representing a 50% stress difference <sup>12)</sup>. Similarly, for AISI 4340 steel, the peak stress varies from 55MPa to 70MPa, approximately, representing a 27% stress increase <sup>29)</sup>. Furthermore, the occurrence of softening mechanisms, crucial for good workability, appears to be at lower strain rates i.e. higher temperatures than other steels. The above findings can be related to the occurrence of DRX at higher temperature and/or lower strain rates in the present steel (**Fig. 5**), as compared to similar steels but with a lower Nickel content. Furthermore, the higher strain rate sensitivity of nickel-modified AISI 4330 steel can explain the higher  $\alpha$  value determined in this study (**Table 4**). The strain rate sensitivity and the change in the DRX occurrence conditions can be related to the nickel content. Non-alloyed austenite has low stacking fault energy (SFE) ( $-390 \text{ mJ.m}^{-2}$ ), and therefore, a strong tendency for

DRX. By alloying the austenite, the stacking fault energy increases and therefore the dislocation motion is reduced<sup>17, 27, 29, 37)</sup>. As a result, the temperature and strain rate range for DRX occurrence are reduced<sup>12, 17)</sup>. Specifically, a 4%wt nickel alloying of pure iron increases the SFE to approximately 150 mJ.m<sup>-2</sup>, which highlights the strong effect of nickel on SFE, as compared to chromium (30 mJ.m<sup>-2</sup>) and manganese (20 mJ.m<sup>-2</sup>)<sup>37)</sup>.

Moreover, it has been reported that the presence of nickel promotes cross slip and increases the dislocation density<sup>1, 38)</sup> which contributes to increase the toughness of the material. As a result, the stress multiplier,  $\alpha$ , for nickel-modified AISI 4330 steel is higher of about 50% than low alloyed steels (**Table 4**). In contrast, its strain rate sensitivity increased significantly as shown in **Fig. 12**.

The increase in SFE implies that higher energy is needed to initiate DRX in the material. Experimentally, this corresponds to a higher strain for the initiation of DRX and/or a higher DRX start temperature in the nickel-modified AISI 4330 steel ( $\epsilon=0.3$ ), as compared to the conventional Cr-Ni-Mo steel ( $\epsilon=0.2$ )<sup>29)</sup> under the same deformation conditions (**Table 5**). As reported in Table 3, the DRX start temperature at 0.1s<sup>-1</sup> strain rate is higher for nickel alloyed steel than for the two other steels : 1373K for nickel-modified AISI 4330 steel, 1223K and 1273K for Cr-Ni-Mo steel and Cr-Ni-Mo-Nb steels, respectively. The Avrami's constant  $k$  decreases from 0.695 to 0.5504 with nickel alloying (**Fig. 11**), and based on Eq. (11), the nucleation and the growth rates of recrystallized grains in nickel-modified AISI 4330 steel are reduced. Moreover, as it can be seen in **Table 5**, Avrami's constant  $n_{\text{DRX}}$  is around 2 for Cr-Ni-Mo-Nb and 34CrNiMoV steel, indicating a grain-edge nucleation after substructure formation during hot deformation. However, the Avrami's constant for nickel-modified AISI 4330 steel is

about 4, which imply that the nucleation rate is constant<sup>39)</sup>. As a result, it can be said that nickel alloying reduces the nucleation and grain growth while keeping it constant. These observations are in agreement with the increase in the DRX start temperature and the stress multiplier increase at higher nickel contents.

It has been reported that the apparent activation energy is mainly stress-dependent<sup>17, 40)</sup>; therefore, an increase in the steady-state stress is indicative of higher activation energy. Microalloying elements are known for delaying recrystallization<sup>36)</sup>; however, the influence of vanadium on the activation energy and flow stress of medium carbon low alloyed steels has been reported to be negligible<sup>13, 14, 36)</sup>. Therefore, solid solution strengthening elements such as copper, nickel or manganese can be identified as the root causes of the observed increase in the steady-state stress, and consequently, the apparent activation energy decrease observed in the investigated alloy<sup>41, 42)</sup>. Pickering established the strengthening effect coefficients for solid solution elements, including manganese, copper and nickel<sup>41)</sup>. In the composition of our steel, the nickel content is significantly higher than that of Mn and Cu, which implies that nickel has a preferential strengthening effect after carbon, as reported in **Table 6**. Therefore, the lower kinetics of DRX of nickel-modified AISI 4330 steel can essentially be attributed to the solid solution strengthening effect of nickel<sup>41, 42)</sup>.

It has been reported by Saxena *et al.*<sup>5)</sup> that AISI 4330 steel grade possess high toughness and excellent fatigue crack growth resistance, which is a result of its chemistry and metastable microstructure obtained after heat treatment. Although nickel alloying enhances the toughness of the steel as well as decreases the ductile-fragile temperature transition<sup>1)</sup>, the reduction of DRX kinetics and DRX temperature lead to lower

workability of these steels compared to non-nickel alloyed steels. Such reduction can imply that during hot deformation, DRX occurs on faces of the sample whereas DRV only occurs at the edges. For example, as it can be seen on **Fig. 5c**, by increasing the temperature from 1423K to 1473K, DRX occurs instead of DRV, changing therefore the stress level. Thus, as DRX lowers the stress level, cracks can grow from these recrystallized zones due to tension generated between DRV zones and DRX zones. This mechanism is similar to adiabatic shear bands (ASB) generated under high speed impact as observed by Polyzois *et al.* <sup>43)</sup> on AISI 4340 steel. Cracks appeared on ASB characterized by small recrystallized grain size after impact. ASB is surrounded by severe elongated grains, indicating that DRX occurrence between DRV zones resulted in softening that led to excessive tension into the material and therefore cracking.

## 5. Conclusions

Isothermal hot compression tests were conducted on nickel-modified AISI 4330 steel over a wide range of strain rates ( $0.01 - 1s^{-1}$ ) and temperatures (1223 – 1523K). Experimental flow curves show softening mechanisms such as dynamic recrystallization and dynamic recovery. The calculated apparent activation energy and kinetics of recrystallization were compared with those of other low alloyed steels. The conclusions of the present study can be summarized as follows:

1. The addition of nickel increases the apparent activation energy and, by extension, the DRX start temperature and stress levels.

2. Increasing the nickel content from 0 to 2.89 %wt decreases the apparent activation energy from 490.749 to 367.927 kJ.mol<sup>-1</sup>. Material constants, alpha and n are however higher and lower respectively compared to low alloyed steels.
3. The Avrami kinetics of dynamic recrystallization were studied, k and n<sub>DRX</sub> values were determined, and the Avrami equation can be written as:

$$X = 1 - \exp(-0.5504t^{4.1798})$$

The developed model shows good agreement with experimental results.

4. A higher nickel content does not appear to affect grain growth during recrystallization.
5. As the Avrami k value is lower for nickel-modified AISI 4330 steel than low alloyed steels, it indicates that the kinetics of nucleation is slower with nickel alloying.
6. Strain rate sensitivity of the nickel-modified AISI 4330 steel is significantly higher than that of similar steels with a lower Nickel content. The addition of nickel therefore modifies the flow behavior of the steel and reduces its high temperature formability to minimal strain rate change.

## References

- 1) J. R. Davis : Alloying. Understanding the Basics, ASM International, Materials Park, OH, (2001), 123.
- 2) H. Chandler : Heat Treater's Guide: Practices and Procedures for Irons and Steels, ASM international, Materials Park, OH, (1994), 347.
- 3) Z. Y. Liu, X. L. He, J. Q. Chen, S. W. Yang, B. W. Chen, M. Hu and W. Liang : *Adv. Mat. Res.*, **295**(2011), 1436.
- 4) J. S. Lee and J. S. Chun : *J. Mat. Sci.*, **16**(1981), 1557.
- 5) V. K. Saxena, G. Malakondaiah, V. M. Radhakrishnan and P. R. Rao : *Scr. Metall. Mater.*, **28**(1993), 1257.
- 6) F. Nürnberger, O. Grydin, M. Schaper, F. W. Bach, B. Koczurkiewicz, and A. Milenin : *Steel Res. Int.*, **81**(2010), 224.
- 7) M. Mirzaee, H. Keshmiri, G. R. Ebrahimi and A. Momeni. : *Mater. Sci. Eng. A*, **551**(2012), 25.
- 8) S. Barella, A. Gruttadauria, C. Mapelli, D. Mombelli, C. L. Fanezi, F. Fioletti, M. Formentelli and M. Guarneri : *Adv. Eng. Mater.*, **16**(2014), 103.
- 9) M. Bitterlin, A. Loucif, N. Charbonnier, M. Jahazi, L. P. Lapierre-Boire and J. B. Morin : *Eng. Fail. Anal.*, **68**(2016), 122.

- 10) N. Bandyopadhyay, C. L. Briant and E. L. Hall : *Metall. Mater. Trans. A*, **16**(1985), 721.
- 11) B.M. Connolly, J. Paules and A. DeArdo : *Metall. Ita.*, **1**(2015), 3.
- 12) S. V. Sajadifar, G. G. Yapici, M. Ketabchi, and B. Bemanizadeh : *J. Iron Steel Res., Int.*, **20**(2013), 133.
- 13) H. L. Wei, G. Q. Liu and M. H. Zhang : *Mater. Sci. Eng. A*, **602**(2014), 127.
- 14) W. F. Shen, L. W. Zhang, C. Zhang, Y. F. Xu and X. H. Shi : *J. Mater. Eng. Perform.*, **25**(2016), 2065.
- 15) S. L. Zhu, H. Z. Cao, J. S. Ye, W. H. Hu and G. Q. Zheng : *J. Iron Steel Res., Int.*, **22**(2015), 264.
- 16) H. Y. Li, Y. H. Li, X. F. Wang, J. J. Liu and Y. Wu : *Mater. Des.*, **49**(2013), 493.
- 17) H. J. McQueen and N. D. Ryan : *Mater. Sci. Eng. A*, **322**(2002), 43.
- 18) B. L. Bramfitt and A. O. Benschoter : *Metallographer's Guide, Practices and Procedures for Irons and Steels*, ASM International, Materials Park, (2002), 302.
- 19) Q. Guo-Zheng : *Recent Developments in the Study of Recrystallization*, ed. by P. Wilson, InTech, Vienna, (2013), 61.
- 20) J. Rasti, A. Najafizadeh, M. Meratian : *Int. J. ISSI*, **8**(2011), 1, 26.
- 21) H. Monajati, A. K. Taheri, M. Jahazi and S. Yue : *Metall. Mater. Trans. A*, **36**(2005), 895.

- 22) Y. P. Li, E. Onodera and A. Chiba : *Metall. Mater. Trans. A*, **41**(2010), 224
- 23) G.E. Dieter : *Mechanical Metallurgy*, McGraw-Hill, New York, (1988), 539.
- 24) E. I. Poliak and J. J. Jonas : *Acta Mater.*, **44**(1996), 127.
- 25) J. J. Jonas, X. Queleñec, L. Jiang and E. Martin : *Acta Mater.*, **57**(2009), 2748.
- 26) T. Sakai, A. Belyakov, R. Kaibyshev, H. Miura and J. J. Jonas : *Prog. Mater. Sci.*, **60**(2014), 130.
- 27) C. Zhang, L. Zhang, Q. Xu, Y. Xia and W. Shen : *Mater. Sci. Eng. A*, **678**(2016), 33.
- 28) D. A. Porter and K. E. Easterling : *Phase Transformations in Metals and Alloys (Revised Reprint)*, Springer Science + Business Media, B.V., Dordrecht, (1992), 287.
- 29) C. Zhang, L. Zhang, W. Shen, C. Liu, Y. Xia and R. Li : *Mater. Des.*, **90**(2016), 804.
- 30) S. V. Sajadifar, M. Ketabchi and M. R. Nourani : *J. Iron Steel Res., Int.*, **17**(2010), 65.
- 31) H-L. Wei, G-Q. Liu, H-T. Zhao, and M-H. Zhang : *Mater. Sci. Eng. A*, **596**(2014), 112.
- 32) H. W. Mead and C. E. Birchenall : *J.Met.*, **8**(1956), 1336.
- 33) T. Sakai and M. Ohasi : *Tetsu-to-Hagané*, **67**(1981), 2000.

- 34) T. Matuszewski, P. M. Machmeier and H. J. McQueen : *Metall. Trans. A*, **22**(1991), 469.
- 35) B. X. Wang, X. H. Liu and G. D. Wang : *Mater. Sci. Eng. A*, **393**(2005), 102.
- 36) M. G. Akben, B. Bacroix and J. J. Jonas : *Acta Metall.*, **31**(1983), 31.
- 37) K. R. Limmer, J. E. Medvedeva, D. C. Van Aken and N. I. Medvedeva : *Compu. Mater. Sci.*, **99**(2015), 253.
- 38) K. H. Lee, S. G. Park, M. C. Kim, B. S. Lee and D. M. Wee : *Mater. Sci. Eng. A*, **529**(2011), 156.
- 39) R. D. Doherty : *Physical Metallurgy*, Vol. 2, ed. by R. W. Cahn and P. Haasen, North-Holland, Amsterdam, (1996), 1435.
- 40) A. Laasraoui and J. J. Jonas : *Metall. Trans. A*, **22**(1991), 1545.
- 41) F. B. Pickering : *Materials Science and Technology: a Comprehensive Treatment*, Vol. 7, ed. by R.W. Cahn, P. Haasen, E. J. Kramer and F. B. Pickering, VCH, Weinheim, (1992), 41.
- 42) S. Vervynckt, K. Verbeken, B. Lopez and J. J. Jonas : *Int. Mater. Rev.*, **57**(2012), 187.
- 43) I. Polyzois and N. Bassim : *Mater. Sci. Eng. A*, **631**(2015), 18.

## Table Captions

<b>C</b>	<b>Ni</b>	<b>Cr</b>	<b>Mo</b>	<b>Mn</b>	<b>Si</b>	<b>Al</b>	<b>Cu</b>	<b>V</b>	<b>P</b>	<b>S</b>	<b>N</b>
0.33	2.89	1.08	0.48	0.53	0.25	0.029	0.2	0.063	0.015	0.004	0.0045

Table 1 : Chemical composition of nickel-modified 4330 steel (% wt)

<b>Reagents</b>	<b>Composition</b>	<b>Time</b>
Marshall	8g oxalic acid, 5mL H <sub>2</sub> SO <sub>4</sub> , 100mL H <sub>2</sub> O, H <sub>2</sub> O <sub>2</sub> (30%)	15 sec
Nital 3% wt	3mL HNO <sub>3</sub> , 97mL C <sub>2</sub> H <sub>6</sub> O	20 sec
Nitrosulfuric acid	20mL HNO <sub>3</sub> , 10mL H <sub>2</sub> SO <sub>4</sub> , 70mL H <sub>2</sub> O	3 sec

Table 2 : Etchants used to reveal microstructure on deformed samples <sup>18)</sup>

	Strain rate ( $\dot{\epsilon}$ )			
	0.01	0.1	0.5	1
Temperature (K)				
1223	DRX	DRV	DRV	DRV
1273	DRX	DRV	DRV	DRV
1323	DRX	DRV	DRV	DRV
1373	DRX	DRV	DRV	DRV
1423	DRX	DRX	DRV	DRX
1473	DRX	DRX	DRX	DRV
1523	DRX	DRX	DRX	DRX

Table 3 : Occurrence of DRX and DRV in nickel-modified AISI 4330 steel

Steel Grade	Ref.	Composition (%wt)				Stress multiplier $\alpha$ (MPa <sup>-1</sup> )	Stress exponent n	Apparent activation energy $Q_{act}$ (kJ.mol <sup>-1</sup> )	T°K DRX ( $\dot{\epsilon}=0.1$ s <sup>-1</sup> )
		C	Ni	Cr	Microall.				
AISI 4130	30	0.33	0	1	-	0.01	7.077	490.749	1173
AISI 4340	12	0.41	1.82	0.72	-	0.012	7.74	427.2	1173
AISI 4330 mod.	Present	0.33	2.89	1.08	V = 0.063	0.0150	4.2360	367.927	1373

Table 4 : Influence of nickel on apparent activation energy and stress constants

Steel Grade	Ref.	Composition (%wt)				Avrami constant k	Avrami exponent $n_{DRX}$	T°K DRX ( $\dot{\epsilon}=0.1$ s <sup>-1</sup> )	DRX initiation at $\dot{\epsilon}=0.1$ s <sup>-1</sup> and T=1423 K
		C	Ni	Cr	Microall.				
Cr-Ni-Mo-Nb	15	0.52	0.72	1.92	Nb = 0.036	0.62	1.84	1273	0.1
34CrNiMo	29	0.36	1.64	1.67	-	0.695	1.897	1223	0.2
AISI 4330 mod.	Present	0.33	2.89	1.08	V = 0.063	0.5504	4.1798	1373	0.3

Table 5 : Influence of nickel on DRX kinetics

$\sigma_{strength} = 680P + 83Si + 32Mn + 38Cu + 33Ni + 5000(C + N)$			
Element	Wt%	Strengthening effect (MPa)	Relative effect (%)
C	0.33	1650	90.5
Ni	2.89	95.37	5.2
N	0.0045	22.5	1.2
Si	0.25	20.75	1.1
Mn	0.53	16.96	0.9
P	0.015	10.2	0.5
Cu	0.2	7.6	0.4

Table 6 : Strengthening effect of solid solution elements of nickel-modified AISI 4330 steel according to Pickering<sup>41)</sup>

## Figures Captions

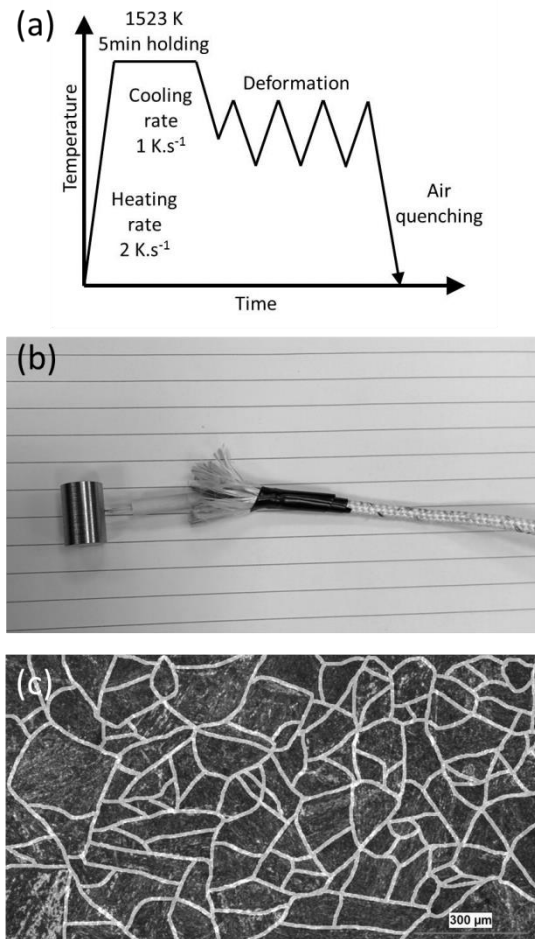


Fig. 1 : (a) Experimental procedure of hot compression test, (b) instrumented compression sample, (c) microstructure of as-forged sample etched with Nital 3% wt.

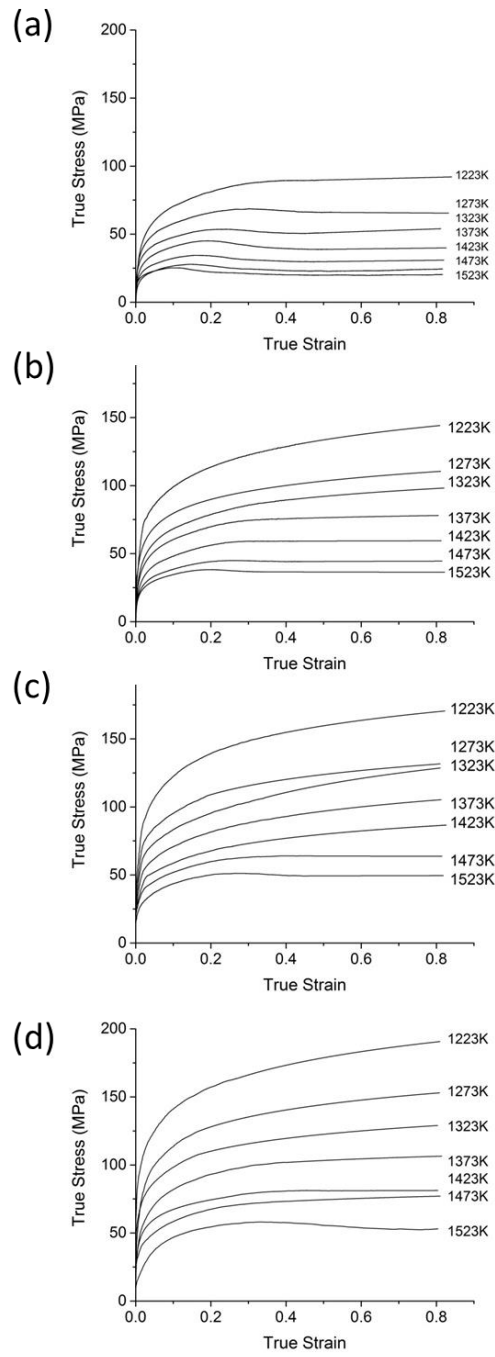


Fig. 2 : Raw strain-stress curves at strain rate of (a)  $0.01 \text{ s}^{-1}$ , (b)  $0.1 \text{ s}^{-1}$ , (c)  $0.5 \text{ s}^{-1}$  and (d)  $1 \text{ s}^{-1}$

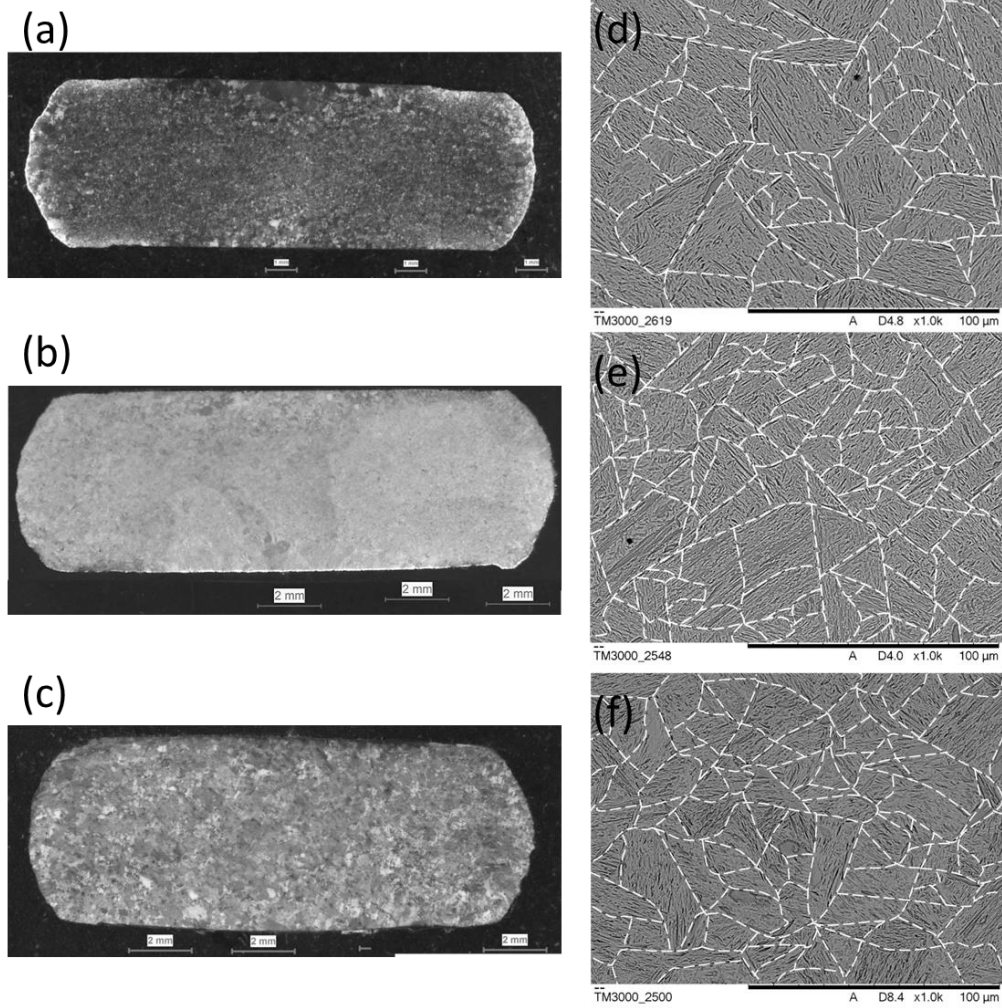


Fig. 3 : Deformed samples (a) at 1473K and  $1s^{-1}$  etched with Nital 3%wt, (b) at 1423K and  $0.01s^{-1}$  with Marshall reagent, (c) at 1523K and  $0.01s^{-1}$  with nitrosulfuric acid. (d, e and f) Respective SEM observation at the center of specimens, white dotted lines highlighting grain boundaries.

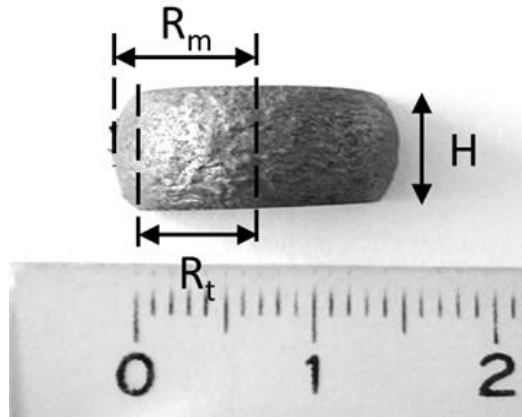


Fig. 4 : Sample after hot compression test at 1223K and  $0.01s^{-1}$

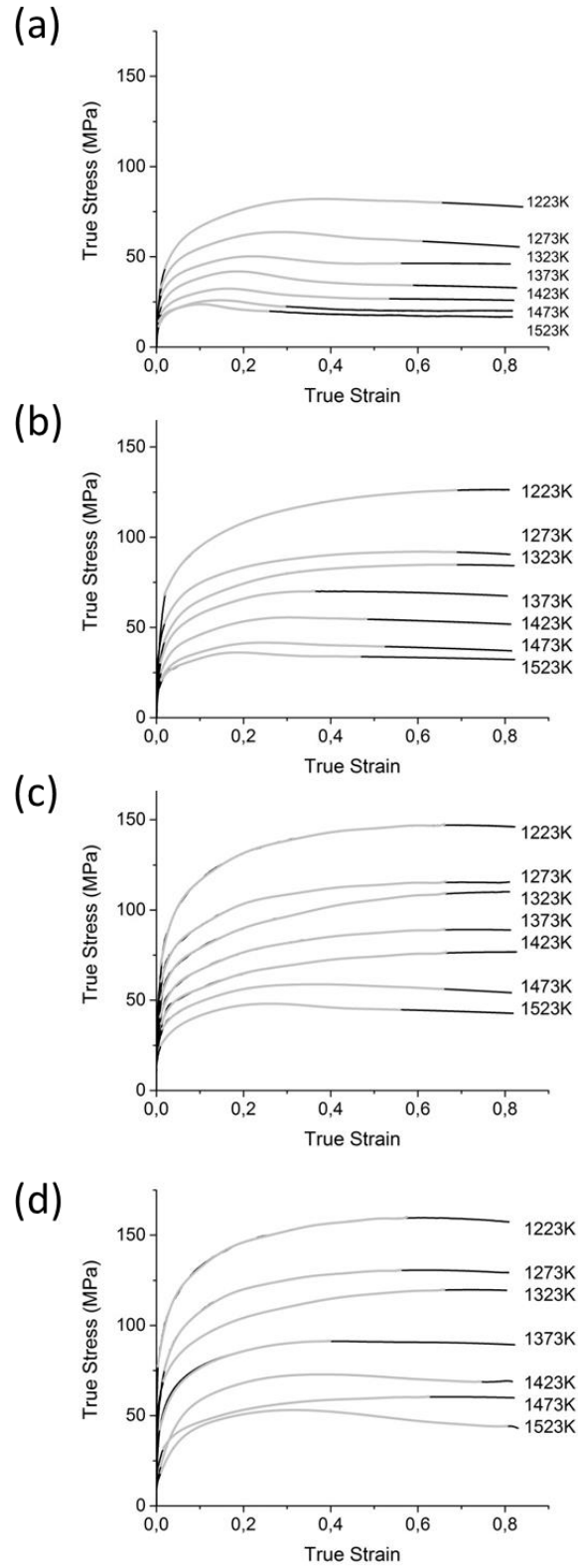


Fig. 5 : Corrected strain-stress curves at strain rate of (a)  $0.01 \text{ s}^{-1}$ , (b)  $0.1 \text{ s}^{-1}$ , (c)  $0.5 \text{ s}^{-1}$  and (d)  $1 \text{ s}^{-1}$ . Gray lines represent 9<sup>th</sup> order polynomial fitting.

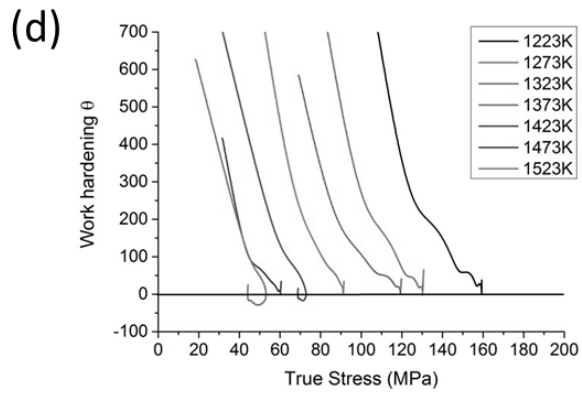
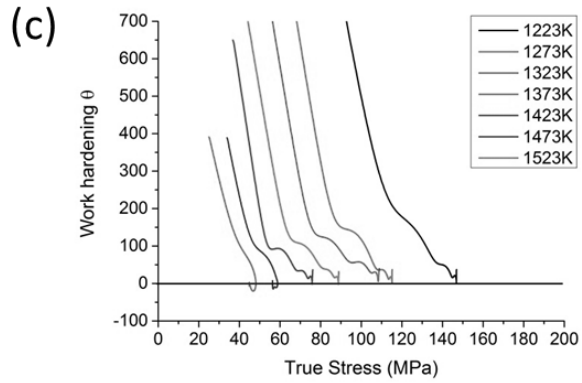
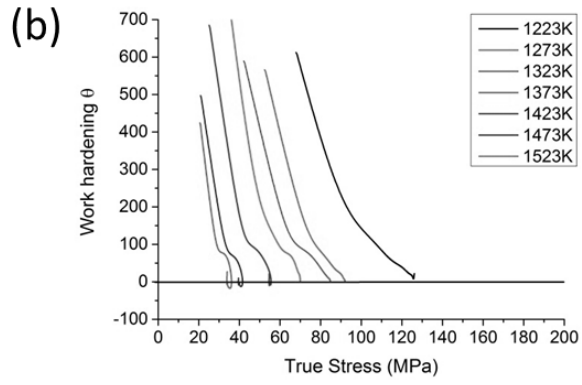
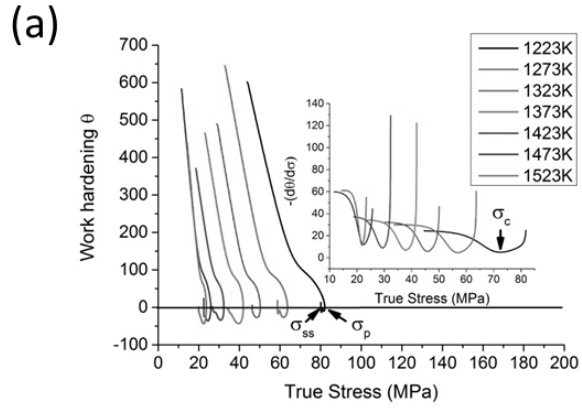


Fig. 6 : Work hardening behavior at strain rate of (a)  $0.01 \text{ s}^{-1}$ , (b)  $0.1 \text{ s}^{-1}$ , (c)  $0.5 \text{ s}^{-1}$  and (d)  $1 \text{ s}^{-1}$ .

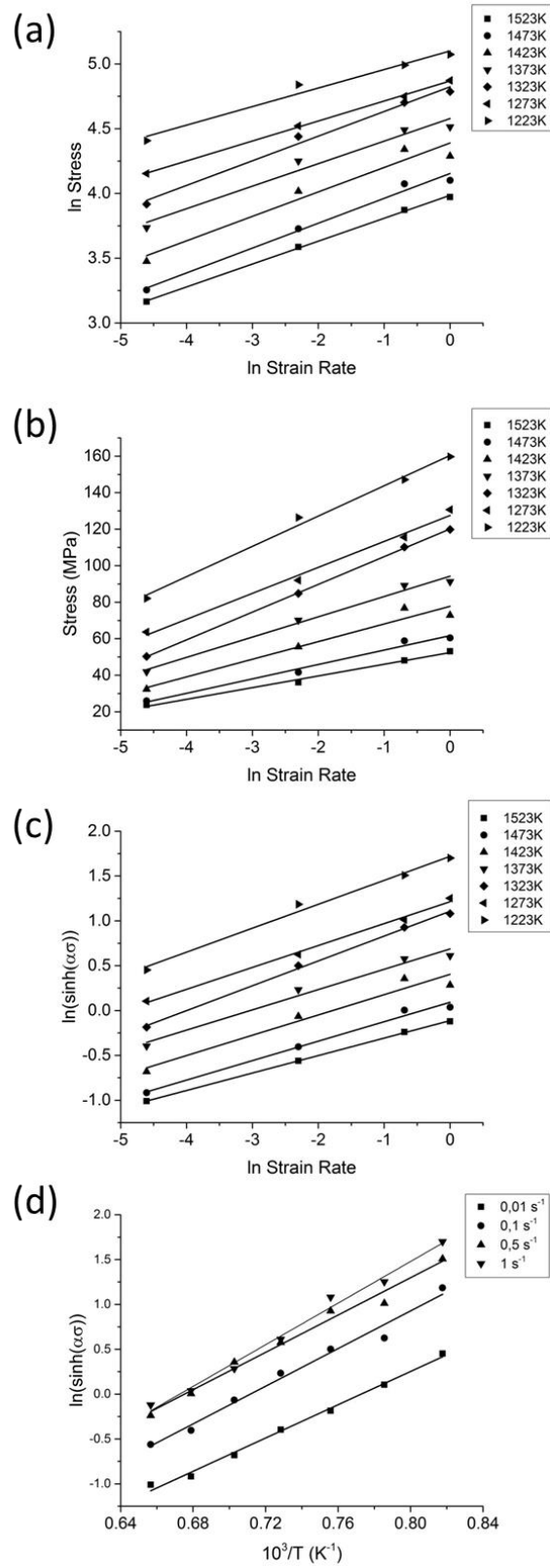


Fig. 7 : Relationships between flow stress, strain rates and absolute temperatures

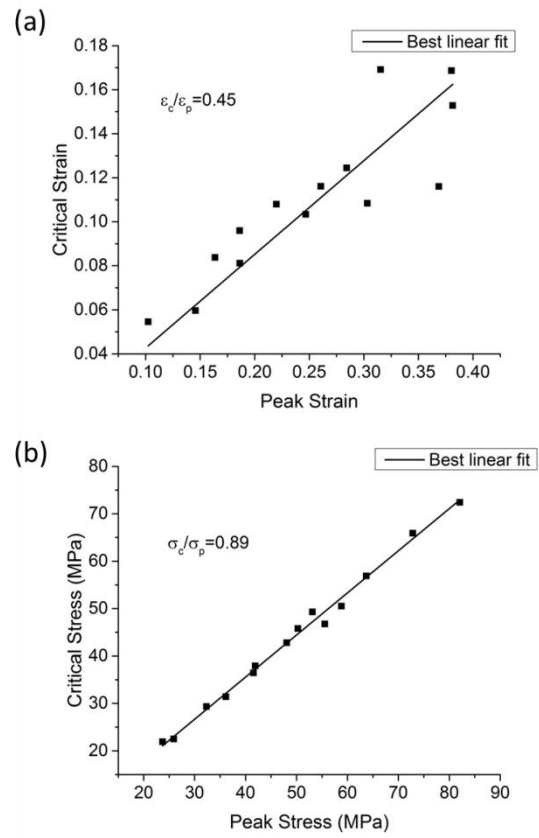


Fig. 8 : Correlation between (a) critical and peak strain and (b) critical and peak stress

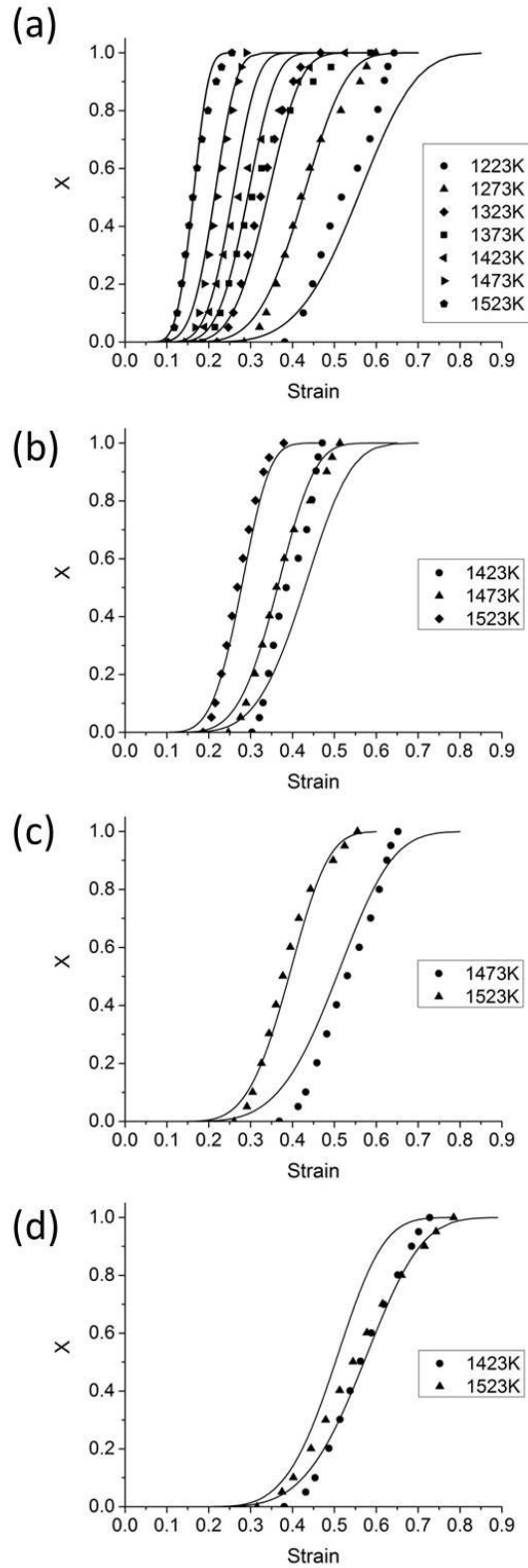


Fig. 9 : Experimental (dots) and predicted (lines) Avrami kinetics of recrystallization for strain rates of (a)  $0.01 \text{ s}^{-1}$ , (b)  $0.1 \text{ s}^{-1}$ , (c)  $0.5 \text{ s}^{-1}$  and (d)  $1 \text{ s}^{-1}$

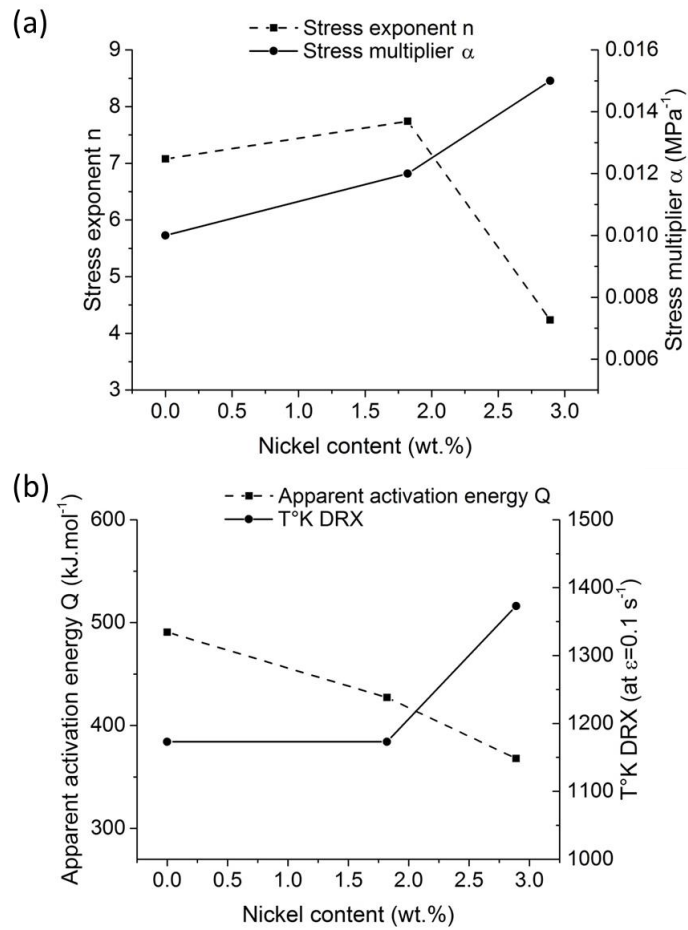


Fig. 10 : (a) Stress exponent  $n$  and multiplier  $\alpha$  and (b) Apparent activation energy  $Q$  and DRX temperature occurrence relative to nickel content

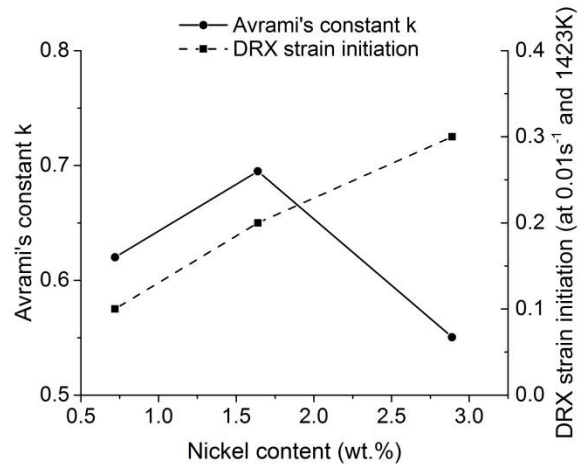


Fig. 11 : Avrami's constant k and DRX strain initiation

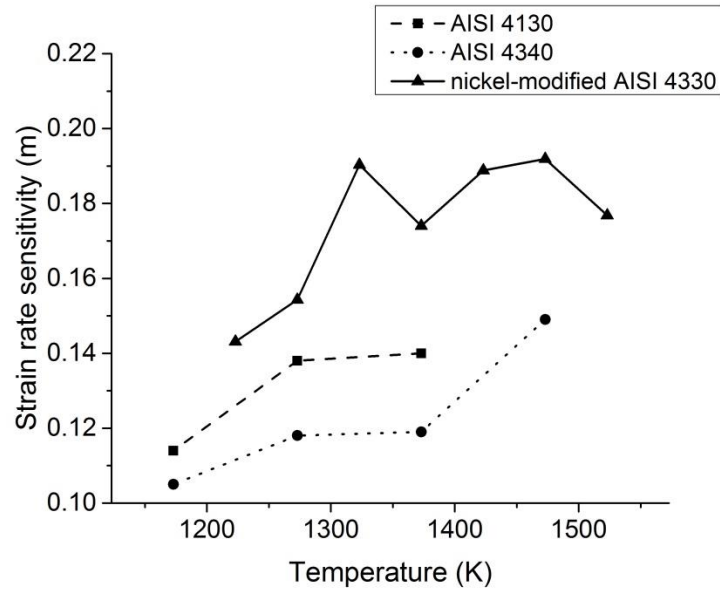


Fig. 12 : Strain rate sensitivity of nickel-modified AISI 4330 steel, AISI 4130 and AISI 4340 steels